Nanoscale

PAPER

View Article Online
View Journal | View Issue

Check for updates

Cite this: *Nanoscale*, 2025, **17**, 22456

Robust electro-mechanical actuation in hydrogenated Xenes leading to reversible topological transition

Sujith Nedungattil Subrahmanian, *[a,b] Nabendu Mondal [a,b] and Joydeep Bhattacharjee [a,b]

Received 30th May 2025,
Accepted 28th August 2025

DOI: 10.1039/d5nr02296g

rsc.li/nanoscale

We report, from first principles, the possibility of reversible onset of the topological insulator (TI) phase in heavier Xanes exclusively through in-plane electro-mechanical actuation. It is found that it is possible to systematically induce robust uniaxial strain through non-uniform application of bias using gates of realizable length-scales. This causes substantial lowering of the band-gap across all Xanes, eventually evolving through weak and strong topologically insulating phases in heavier Xanes, namely germanane and stanane, promisingly within the range of bias sustained by the monolayers. In the case of nano-ribbons of heavier Xanes, bias applied inhomogeneously across the width promises switchable emergence of the TI phase over a fraction of the width and thereby topologically protected interface states, which can be chosen to localize anywhere across the half-width of the ribbon. The demonstrated electro-mechanical actuation and the associated topological tuning of the band-structure, thematically verified in gapped-graphene-based representative systems within the Kane–Mele model with collinear spins, should be possible in the broader class of two-dimensional covalent networks made of elements from the p-block.

Open Access Article. Published on 29 August 2025. Downloaded on 5/5/2026 7:59:23 AM.
This article is licensed under a Creative Commons Attribution-NonCommercial 3.0 Unported Licence.

1. Introduction

Efforts to evolve beyond the three-dimensional silicon–metal combination for channel–drain/source assemblies in active elements of electronic circuitry began with graphene about a quarter of a century ago,[1,2] with the promise of a drastic reduction in dimensionality, dissipative loss and weight of devices. The efforts generalized into the broader family of two-dimensional materials constituted by elements of the p-block down the periodic table,[3] namely the Xenes – silicene,[4] germanene,[5] stanene,[6] and further to the chalcogenides[7,8] – and has continued ever more vivaciously in recent years towards harnessing exotic quantum phases[9] to ease the passage of charge and thermal management, which are central to the large-scale integration of processors with fast-increasing density. In this direction, two-dimensional topological insulators (TIs)[10] have been in focus for more than a decade now, on account of the promise of scatteringless conduction through the topologically protected edge-states they host if cut into ribbons.[11] However, sustaining the topological protection under ambient working conditions and in practical device configurations is the key challenge to overcome, wherein modest progress has been reported[12–14] in recent years. In fact, evidence of the possible tunability of topological edge states in germanene[15,16] at room temperature using an electric field is a contemporary matter of interest from the device perspective. TIs with reversible control over the transition between the topological and trivial phases are thus envisaged to be of significant technological interest and are the motivation of this work as well.

With opening of the band gap at the Dirac point upon hydrogenation in both sub-lattices, hydrogenated Xene monolayers (Xanes) – graphane, silicane, germanane and stanane – offer direct band gaps at Γ, with the optical gap being in the visible range for germanane.[17,18] Substitution of H by heavier atoms,[19,20] or appropriate functional groups, combined with biaxial strain,[19,21,22] has been shown to nontrivially modulate the band-gap of Xanes, leading to a topological phase transition in the heavier ones, namely germanane and stanane, driven by the spin–orbit coupling (SOC) of primarily the σ orbitals. Homogeneously strained Xanes are expected to undergo a topological phase transition for the same reason, since a stretched X–X bond would imply an increase in energy of the occupied σ orbitals, taking them closer to the edge of the valence band, which may eventually facilitate band inversion. On account of the increasing strength of SOC from Si to Sn, the degree of strain required for such a transition progressively

[a]*School of Physical Sciences, National Institute of Science Education and Research Bhubaneswar, Jatni, Odisha 752050, India.*
E-mail: sujith.s@niser.ac.in, sujithb2w@gmail.com
[b]*Homi Bhabha National Institute, Training School Complex, Anushaktinagar, Mumbai 400094, India*

This journal is © The Royal Society of Chemistry 2025

Open Access Article. Published on 29 August 2025. Downloaded on 5/5/2026 7:59:23 AM.
This article is licensed under a Creative Commons Attribution-NonCommercial 3.0 Unported Licence.

decreases from silicane to stanane. As verified in this work for uniaxial strain, the degree of strain required for the transition in case of silicane is as high as above 25%, reducing to almost half of that and further to a quarter in case of germanane and stanane respectively. However, in order to be able to modulate charge passage through matter or vary the degree of their interaction with circularly polarized light, on account of the existence of topologically protected helical edge or interface states, a reversible onset of the TI phase exclusively through reversible physical functionalization is highly desirable. Accordingly, electrically induced onset of topological phases beyond silicane has been proposed for bilayers and multi-layers of Xanes,[23,24] driven by unequal lowering of energies of the s- and p-orbitals in the electric field owing to their even and odd parities, respectively. This leads to a feasible means of achieving band-inversion through application of an electric field uniformly perpendicular to the layers.

Harnessing an electric field as a source of strain, in this work, we report from first principles the use of electro-mechanical actuation as a possible route for controllable onset of weak and strong TI phases in Xanes beyond silicane. Substantial lowering of the band-gap, leading eventually to inversion of valence and conduction band edges at Γ, and thus to onset of a TI phase, is demonstrated computationally in germanane and stanane mono-layers as a result of inhomogeneous strain, induced exclusively through application of an inhomogeneous bias potential through realizable gate configurations. Correspondingly, the possibility of emergence of chiral interface states in Xane ribbons with a realistically applied bias is demonstrated. This work thus brings forth the effectiveness of electro-mechanical actuation in the nontrivial reversible tuning of electronic structures. This facilitates a host of physical and chemical functionalities, ranging from the onset of exotic quantum phases to controlled cleavage of covalent bonds in monolayers of p-block elements, through patterned application of bias.

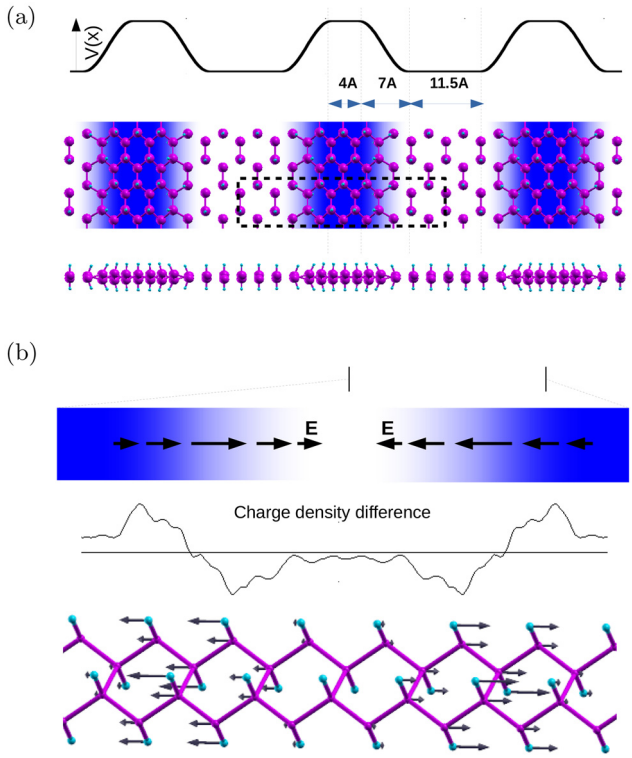

Fig. 1 (a) The applied bias potential and two views of the relaxed structure of the germanane monolayer under the influence of the plotted bias. The unit cell is marked with a black dashed line. The bias (V_{bias}) is kept constant over a length of 4 Å and switched sinusoidally to zero over lengths of 7 Å on two sides. (b) Schematic description of the electric field and difference between charge densities with and without the potential applied. The black arrows in the panel below denote the magnitude of actual displacement with V_{bias} = 1.22 V.

2. Computational details

The primary computation in this work includes: (1) variable cell relaxation of non-uniformly biased supercells of an Xane comprising seven or more unit cells (Fig. 1(a)), (2) fully relativistic calculation of the ground state, and (3) estimation of the $\mathbb{Z}_2$ invariant from the evolution of centres of hermaphrodite Wannier functions (HWFs), as a function of component $\vec{k}$ transverse to the direction of the localization of HWFs.

The electronic structure of the ground state of a given configuration has been computed from first principles using the plane-wave-based implementation of density functional theory (DFT) within the generalized gradient approximation of the PBE exchange-correlation functional, as available in the Quantum Espresso code.[25] Variable-cell structural optimizations have been performed using the Broyden–Fletcher–Goldfarb–Shanno (BFGS) scheme until the forces on each atoms are less than 0.001 Ry au^{-1}. Alternating biased and unbiased regions resembling channels of alternating bias, as realistically applicable using parallel lines of electrodes, have been considered, as shown in Fig. 1(a). Fully relativistic pseudo-potentials allowing non-collinear calculation have been used to compute the band-structure and Kohn–Sham spinor wavefunctions. Semi-core states have been considered in the case of Sn. In all calculations, the k-point grid densities are equivalent to an 18 × 18 × 1 k-mesh for the primitive germanane unit cell.

For estimation of the $\mathbb{Z}_2$ invariant, non-Abelian matrix generalization of the Berry phase is computed for the multitude of occupied bands across the Brillouin zone (BZ), along the two orthogonal directions parallel to reciprocal lattice vectors $\vec{b}_1$ and $\vec{b}_2$ as functions of k_2 and k_1, respectively, where $\{1,2\} \equiv \{x, y\}$. The eigenvalues of the matrices evaluated along $k_x(k_y)$ for a given $k_y(k_x)$ are the centres of the HWF, with maximum localization in $x(y)$ direction but with Bloch-like states in the $y(x)$ direction. Following the Thouless topological pumping[26] of charge, the $\mathbb{Z}_2$ invariant is estimated[27,28] by noting the number of times, the traces of HWFs localized along $x(y)$ direction as a function of $k_y(k_x)$, intersects an arbitrarily shifted $k_y(k_x)$ axis, over half the BZ.

Open Access Article. Published on 29 August 2025. Downloaded on 5/5/2026 7:59:23 AM.
This article is licensed under a Creative Commons Attribution-NonCommercial 3.0 Unported Licence.

For mechanistic understanding of the observed onset or promise of a topological phase, we consider the evolution of the band structures and states at the valence- and conduction-band edges at the TRIM point. We compare them with those in a gapped-graphene monolayer and ribbons at half-filling within the Kane–Mele model,[29] with inhomogeneity in the parameters and without spin mixing. This implies a Hamiltonian of the form:

$$H = \sum_i (m_{\tau_i} + E_i) c_i^\dagger c_i + t \sum_{\langle ij \rangle} (c_i^\dagger c_j + \text{h.c.}) + \lambda \sum_{\langle\langle ij \rangle\rangle} (i c_i^\dagger c_j + \text{h.c.}) \quad (1)$$

for each spin, with the second-neighbour hopping amplitude λ having opposite signs for the two spins. The mass term m_{τ_i} is set to +0.7 eV and −0.7 eV (ref. 30) for the two sublattices (τ). The on-site term E_i and hopping amplitudes t and λ are varied to represent differently biased regions. c_i and c_j are the electron creation and annihilation operators at sites 'i' and 'j' respectively.

3. Results and discussion

In keeping with our aim to study electro-mechanical actuation, we envisage arguably the simplest scenario for the in-plane electric field, as evident in Fig. 1, wherein parallel linear channels of gates embedded under the Xane layer induce an in-plane component of the electric field perpendicular to the gates. Voltage is smoothly switched from the unbiased region (marked in white) to the positively biased region (marked in blue) using a cosine function. Notably, bias from here onwards is always referred to with respect to positive charge. The resultant electric field varying perpendicularly to the gates would thus cause varying uniaxial strain in the same direction, as evident in the relaxed structure shown in Fig. 1(a). Unit cells are thus relaxed parallel to the bias channels in order to allow Poisson's ratio to take effect.

3.1. Electrically induced strain in Xanes

To understand the observed distribution of strain in the X–X bonds implied by the relaxed structure, we note that a covalent bond manifests itself in terms of interatomic sharing of electrons. The shared charge directly determines the bond-order, as introduced by Mayer,[31] implying a quantification of the "strength" of a covalent bond. As is evident from the charge density difference in Fig. 1(b), there are two different types of electron transfer – one is grossly bias-driven from regions of lower to higher bias, which are unbiased and positively biased regions in this work, and the other occurs locally within the region of switching of bias under the influence of an in-plane electric field present in that region. Roughly in one half of the switching region, electrons accumulate on the bonds, while in the other half, the bonds get depleted of charge. The resultant accumulation (depletion) of charge between two nearest atoms would in turn imply an increase (reduction) in the amount of charge shared between atoms, leading to increased (reduced) proximity of the two coordinating atoms. This is evident in the degree of displacement of atoms upon relaxation, shown by the black arrows in the panel at the bottom of Fig. 1(b), where the displacements of the H atoms are caused by the force on the electrons in the Ge–H bond. Thus, the narrower the region of switching, the higher will be the degree of strain. On the other hand, the variation in bond-order on account of the bias-driven gross transfer of electrons results in shorter (longer) bonds in the region of higher (lower) bias, causing an overall displacement of the atoms in the switching region away from lower bias. This also importantly implies that the larger the inequality between the widths of the regions of lower and higher bias, the larger the strain in the bonds in the shorter region. Thus, a rapidly increasing tensile strain with narrowing of the width of the region of lower bias paves the way for selected cleavage of bonds.

Based on the orientation of the X–X bonds w.r.t the direction of the electric field, we expect the b2 bonds (marked in Table 1) to be subjected to maximum uniaxial strain due to an electric field applied in the armchair (AC) direction. Meanwhile, with the electric field along the zigzag (ZZ) direction, the b2 bonds being perpendicular to the field will not be directly impacted. Also, arguably, the strain in the b1 bonds (Table 1) due to an electric field along the ZZ direction will be less than that in the b2 bonds with the field along the AC direction. Thus, we expect application of an electric field in the ZZ direction to be more favorable in terms of lower overall strain in the X–X bonds. Indeed, we find that the b2 Ge–Ge bonds cleave around a bias amplitude of 0.68 V for a field in the AC direction, whereas for a field in the ZZ direction, the bonds can sustain a bias amplitude in excess of 1.5 V. The bond length distribution plotted in Fig. 2 for an electric field in the ZZ direction shows the degree of strain to be dominated expectedly by the b1 bonds in the region of lower bias, rising to about 12% before cleavage.

The degree of extension (contraction) of the b1 bond length increases (decreases) in the region of lower (higher) bias with increasing bias difference. This slowing down of bond contraction in the higher-bias region is because of a rapid increase in Coulomb repulsion in the contracting bonds.

3.2. Choice of direction of effective field

As a precursor to discussion of topological transitions due to electrically induced strain, we first compare (Table 1) the degree of uniform uniaxial strain in the armchair (AC) and zigzag (ZZ) directions required to induce a topological transition in sheets of germanane and stanane within the PBE exchange-correlation. With biaxial tensile strain, germanane is reported to undergo a topological transition with strain of around 10%–12%,[19,32] whereas stanane is expected to require a strain of about 8%.[18,33] As summarized in Table 1, onset of the TI phase in germanane (stanane) occurs between 10% and 12% (4% and 5%) strain in the unit cell along the ZZ direction, which results in about 5% (1.5%) strain in the two b1 bonds and less than 1% strain in the b2 bonds. Meanwhile, for strain

 This journal is © The Royal Society of Chemistry 2025

Open Access Article. Published on 29 August 2025. Downloaded on 5/5/2026 7:59:23 AM.
This article is licensed under a Creative Commons Attribution-NonCommercial 3.0 Unported Licence.

Table 1 Topological transition and strain (%) in bonds as a function of uniaxial strain along the AC and ZZ directions

		Germanane						Stanane					
	Strain	Strain applied along ZZ			Strain applied along AC			Strain applied along ZZ			Strain applied along AC		
In a_x	8	10	12	14	−1.26	−1.58	−1.76	−1.92	2	3	4	5	−1.73	−1.96	−2.17	−2.39
In a_y	−1.70	−2.11	−2.51	−2.94	8	10	12	14	−1.80	−2.07	−2.36	−2.63	2	3	4	5
In b1	3.56	4.48	5.43	6.50	1.48	1.98	2.36	2.72	0.35	0.71	1.09	1.48	−0.16	0.01	0.19	0.38
In b2	0.29	0.46	0.64	0.66	4.90	5.96	7.52	9.20	−0.45	−0.39	−0.34	−0.29	0.64	1.11	1.61	2.12
Type	OI	OI	TI	TI	OI	TI	TI	TI	OI	OI	OI	TI	OI	OI	TI	TI

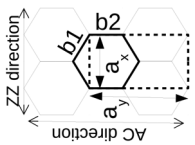

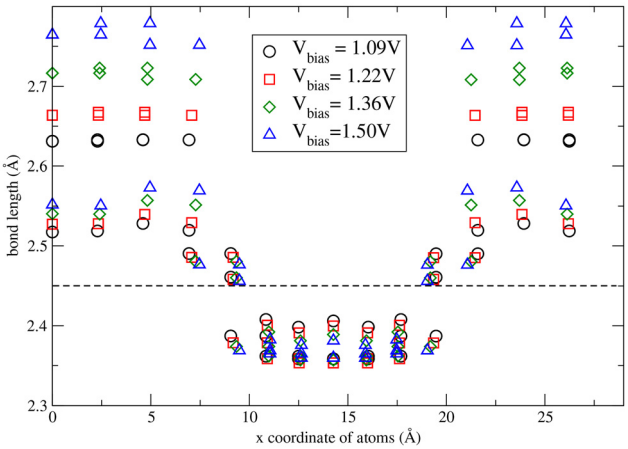

Fig. 2 Ge–Ge bond lengths around each Ge atom across the relaxed germanane supercell (Fig. 1(a))for different bias amplitudes (V_{bias}) with the resultant in-plane electric field component in the zigzag direction.

along the AC direction, the transition occurs between 8% and 10% (3% and 4%) strain in the unit cell, leading to about 6% (1.5%) strain in the b2 bonds and 2% (less than 1%) strain in the b1 bonds. Thus, although the degree of uniaxial strain required for the onset of the TI phase is lower if applied along the AC direction, the degree of resultant strain in the individual bonds at the onset of the TI phase is non-nominally higher than that required if strain is applied along the ZZ direction, more so for germanane than for stanane.

This is also evident from the fact that the contraction of the unit cell in the transverse direction is consistently larger in the case of ZZ strain, implying higher mitigation of the applied tension. Thus, from the perspective of overall strain in the bonds required for the onset of the TI phase, mechanically induced strain along the ZZ direction appears to be a more favorable scenario. In fact, strain along the ZZ direction that is induced electrically has been already discussed above to be favorable in terms of sustaining structural integrity. We therefore here onwards in this work consider the electric field in the ZZ direction as applicable through bias channels in the AC direction (Fig. 1(a)).

As a comment on the nature of the strain in the bonds listed in Table 1 in response to the applied stress, we note that the degree of applied strain and the behavior of bonds transverse to the applied strain, primarily for ZZ, behave differently. Due to the positive Poisson ratio evident in both the systems from the contraction of the unit cell transverse to the applied tensile strain, nominally we expect a contraction of the bonds transversely as well, as indeed seen in the case of stanane. However, it also depends on the strength of individual X–X bonds. The Sn–Sn bond is longer and known to be weaker than the Ge–Ge bond due to the size of the atoms. This means that upon ZZ strain, the b1-type Ge–Ge bonds are expected to stretch by a smaller degree than their Sn–Sn counterparts, which will force a wider Ge–Ge–Ge bond angle made by the b1 bonds and a lesser degree of contraction of the b2-type Ge–Ge

Open Access Article. Published on 29 August 2025. Downloaded on 5/5/2026 7:59:23 AM.
This article is licensed under a Creative Commons Attribution-NonCommercial 3.0 Unported Licence.

bonds compared to those in stanane. In fact, we indeed find the Ge–Ge–Ge bond angle made by the b1 bonds to surpass 120° with increasing strain while it remains well within 120° for stanane, corroborating the result that the Ge–Ge b2 bond actually stretches instead of contracting as in stanane.

3.3. Topological transition in electrically strained Xane supercells

Substantial lowering of the band gap (Fig. 3(a)) all the way to gap closure and eventual inversion of bands is observed as a function of increasing magnitude of the bias difference. As is evident from the evolution of the centres of the HWFs (Fig. 4(a)) in germanane, onset of a *weak* TI phase occurs with the bias potential between 1.22 V and 1.36 V, marked by $\mathbb{Z}_2$ oddness only for HWFs localized in the $\hat{x}$ direction as a function of k_y, consistent with the band inversion observed in the same direction (Fig. 3a). $\mathbb{Z}_2$ oddness as a function of k_x is observed at 1.50 V (Fig. 4(b)), marking the onset of a full TI phase. The bond lengths plotted in Fig. 2 for germanane suggest that the emergence of the TI phase occurs after the tensile (contractile) strain in the b1 bonds in the lower-bias (higher-bias) region exceeds 10% (4%), amounting to an average tensile strain of about 5%. This is consistent with the strain reported in Table 1 to be necessary for emergence of the TI phase under homogeneous uniaxial strain along the ZZ direction. Stanane turns into a full TI with a bias potential of 0.27 V (Fig. 5), marked by $\mathbb{Z}_2$ oddness due to evolution of the HWCs in both the $\hat{x}$ (Fig. 5b (upper)) and $\hat{y}$ (Fig. 5b (lower)) directions, with about 3.5% average tensile strain, consistent with that reported in Table 1.

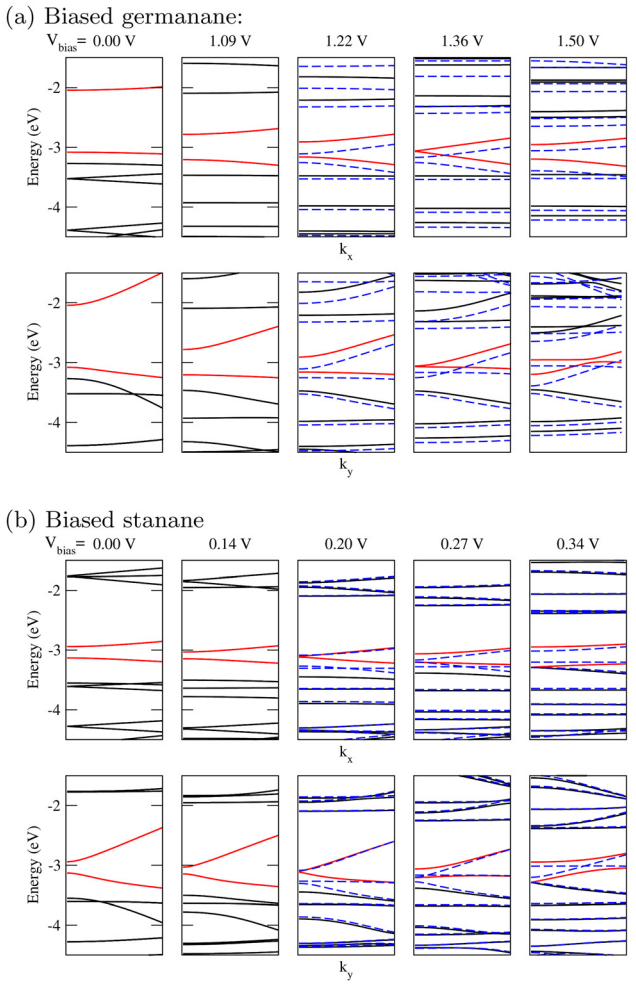

Fig. 3 Band-structures of inhomogeneously biased germanane and stanane, respectively, are plotted in (a) and (b) for a 56-atom orthogonal supercell (Fig. 1). The ranges of k_x and k_y plotted cover a fifth of the respective BZs from Γ. The bands shown in black and red are computed with the SOC applied. The valence and conduction bands are marked in red. The bands shown in dashed blue are computed without any relativistic correction.

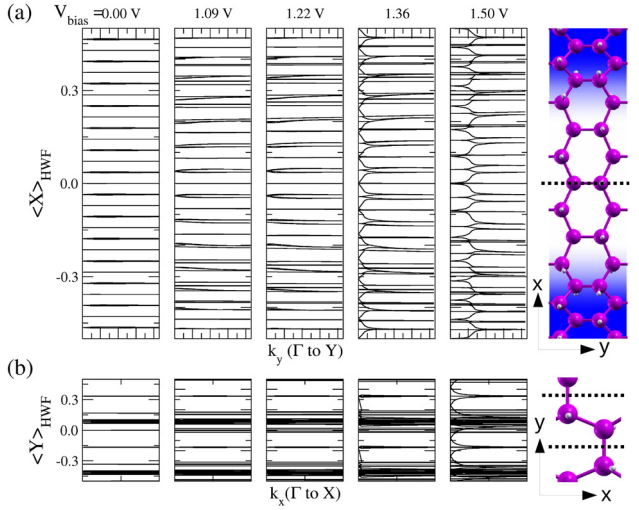

Fig. 4 (a) Centres of HWFs localized along $\hat{x}$ as a function of k_y in the germanane supercell (Fig. 1). (b) Counterpart of (a) for HWFs localized along $\hat{y}$. Locations of atoms are provided as a guide to the eye.

3.3.1. Non-relativistic band inversion. Important from the point of view of detection and application, band inversion at the TRIM(Γ) is also accompanied by spatial swapping of peaks of the valence and conduction band edges (VBE and CBE) at the TRIM. Upon transition to the TI phase, substantial population of the VBE at Γ shifts (Fig. 6(a)) from the region of higher bias to the switching region, and *vice versa* for the CBE, while the nature of the VBE and CBE flips at Γ (Fig. 6(b and c)). The nature of the two bands primarily differs in the presence and absence of nodes of the wavefunctions on the path of X–X nearest-neighbor coordination, expectedly implying a switch of parity. Interestingly, the observed band inversion and swapping of population of the VBE and CBE at Γ are also observed without any relativistic input like spin–orbit coupling (SOC) or relativistic correction to the kinetic energy, implying reasons other than relativistic effects to be responsible for band inversion in the given system. This becomes apparent through comparison of the VBE and CBE in Fig. 6(c) for Γ with those in (e)(i) in the same figure, depicting the VBE and CBE close to Γ computed without relativistic correction post-band-

Open Access Article. Published on 29 August 2025. Downloaded on 5/5/2026 7:59:23 AM.
This article is licensed under a Creative Commons Attribution-NonCommercial 3.0 Unported Licence.

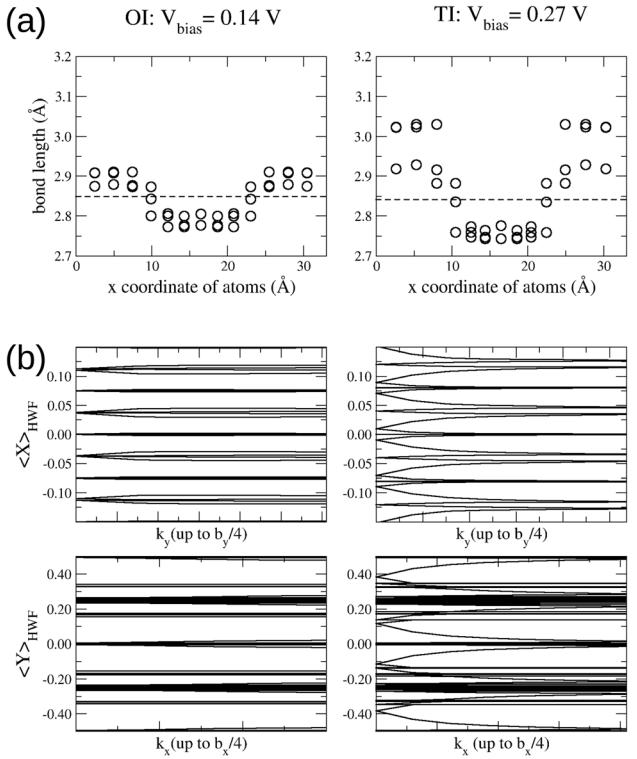

Fig. 5 (a) Sn–Sn bond lengths around Sn atoms across the relaxed stanane supercell, similar to in Fig. 1(a), before and after transition to the TI phase. (b) Centres of HWFs localized along $\hat{x}$ ($\hat{y}$) in the upper (lower) panels as a function of k_y (k_x), spanning over a quarter of the BZ in the respective directions. Plots in the left (right) column correspond to V_{bias} = 0.14 V (0.27 V).

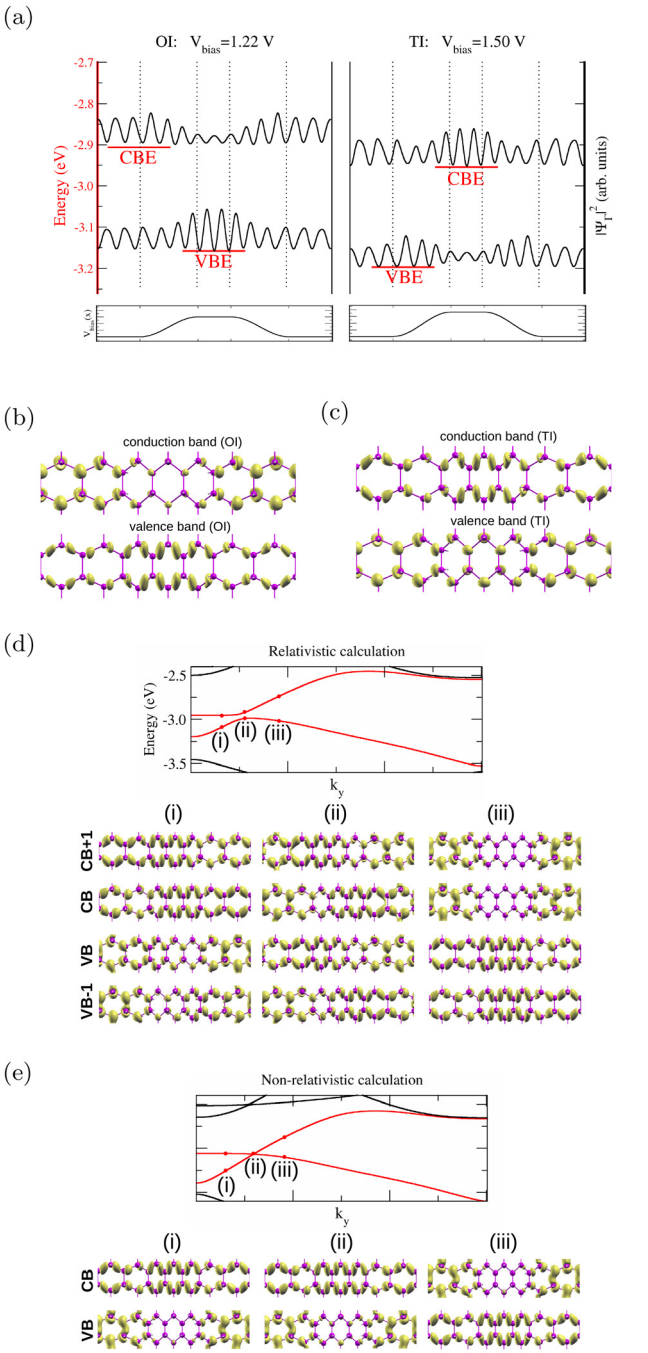

Fig. 6 (a) Projection of the VBE and CBE at the TRIM(Γ) in the $\hat{x}$ direction for the germanane supercell (Fig. 1(a)) before and after the TI transition. VBE and CBE at Γ for (b) OI at 1.22 V and (c) TI at 1.50 V. VBE and CBE plotted at different k-points from (d) fully relativistic and (e) non-relativistic calculations for V_{bias} = 1.50 V.

inversion at Γ. As indicated by the band structure shown in dashed blue in Fig. 3, with a non-relativistic pseudo-potential, gap-closure happens at Γ at a bias close to that with SOC applied, followed by a narrow gap on the order of meV or less, opening away from Γ. The inversion in fact can be simply understood as an interplay of: (1) the enhanced (restrained) lowering of the VBE due to increased (decreased) strength of electron hopping along contracted (extended) X–X bonds, and (2) the resultant increase (decrease) in on-site energy due to increased (decreased) inter-atomic Coulomb repulsion, owing to an increase (decrease) in the proximity of the X atoms in the contracted (extended) X–X bonds, in the higher-bias (lower-bias) region. Indeed, the hopping parameters and on-site terms for the σ electrons of the Ge atoms computed in the Wannierised basis, constructed following templates of hybrid atomic orbitals[34] directed along nearest-neighbor coordination around the Ge atoms, show a comparable increase (>1 eV) in the biased (1.5 V) region compared to their counterparts in the unbiased region. Accordingly, to demonstrate the lowering of the gap leading to complete inversion at Γ due to the competing non-relativistic tight-binding parameters rooted in the factors anticipated above, we considered a graphene hetero-structured supercell (Fig. 7(a)) with two regions, R1 and R2, with different nn-hopping (t_{nn}), set to −1.0 eV and −1.5 eV, respectively, for a single p_z orbital per site at half-filling. Notably, electrons being negatively charged, the enhancement of the on-site term due to reduced X–X separation in the positively biased region would be partially cancelled by the bias itself. However, such cancellation would not happen in the unbiased region, where the on-site term reduces due to

Open Access Article. Published on 29 August 2025. Downloaded on 5/5/2026 7:59:23 AM.
This article is licensed under a Creative Commons Attribution-NonCommercial 3.0 Unported Licence.

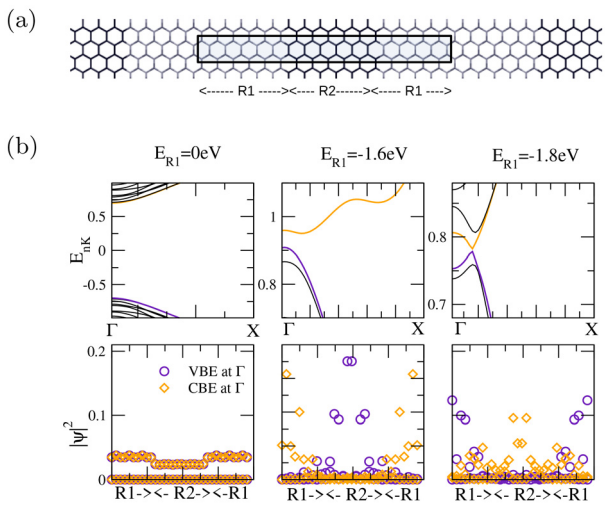

Fig. 7 (a) Unit cell of the gapped-graphene monolayer model system with two regions R1 and R2 per unit cell. (b) Band-structure and charge density of valence and conduction band edges at Γ computed with different on-site terms for region R1.

increased X–X separation. Accordingly, the on-site term E_{R1} is reduced over the sites marked as R1, resembling the unbiased region of the germanane supercell (Fig. 1(a)) with stretched Ge–Ge bonds. Lowering of the band-gap and eventual inversion of the bands at Γ between E_{R1} = −1.6 eV and −1.8 eV is indeed observed (Fig. 7(b)), accompanied with spatial swapping of the VBE and CBE between R1 and R2 in agreement with that observed for non-uniformly biased germanane (Fig. 6 (a–c)).

3.3.2. Role of spin–orbit coupling. To examine the role of SOC, we note that without SOC, the system would have remained an ordinary insulator (OI) with a very narrow gap or in effect a semi-metal. With a fully relativistic pseudo-potential enabling SOC, the gap increases to the order of 0.03 eV after closure at Γ (Fig. 6(d and e)). Without SOC, the nature of the states (Fig. 6(e)) changes abruptly across the narrow gap, implying in effect a band crossing with only nominal mixing of the bands at the point of crossing. With SOC, however, we see substantial and systematic mixing (Fig. 6(d)) in the nature of the wavefunctions across the unit cell. In particular, the states at the gap marked as (ii) in Fig. 6(d) suggest the degenerate pairs constituting the VBEs (and similarly the CBEs) to be equal but out-of-phase mixtures of the two parities characterizing the VBE and CBE at Γ. Thus, although SOC in this system is not responsible for band inversion at the TRIM, it is responsible for mixing of bands of different parities and opening of the gap, leading to onset of the topological phase after band closure at Γ. Thus, it is apparent that if band inversion occurs non-relativistically within the range of bias potential sustained by the system, then a TI phase is likely to exist if SOC consolidates sufficiently in the process to open a gap. The consolidation would occur primarily at the region of lower bias, where stretched X–X bonds would lower the effective hopping of electrons between σ orbitals and bring the corresponding bonding and anti-bonding manifolds sufficiently close enough energetically for the SOC of σ orbitals to take effect. Notably, the presence of an electric field in part of the unit cell breaks the time-reversal symmetry (TRS), implying that the TI phase is a TRS broken quantum spin Hall (QSH) insulator.

3.3.3. Realistic length-scales. We next survey the variability of the onset bias in terms of the widths of the differently biased regions. As already discussed, in order to maximize tensile strain in the lower-bias region, it needs to be narrower. On the other hand, the wider the higher-bias region, the lower the compressive strain and thus the lower the proximity of X atoms crucial for band inversion. Thus, an optimal ratio of widths of the higher- and lower-bias regions is essential for the onset of the TI phase at the lowest bias potential given the length of the supercell, in order to ensure sustainability of the system. Accordingly, we consider the supercell shown in Fig. 1(a) and increase the width of the higher-bias region (d_{bias} in Fig. 8), keeping the supercell length unchanged, and track the onset of the TI phase. The width of the switching region is kept at 7 Å. The variation of the onset of the TI phase as a function of the biased fraction of the supercell and voltage applied is summarised in Fig. 8. As expected, with increasing width of the biased region, $\mathbb{Z}_2$ oddness (marked in red) emerges at a lower positive bias for both directions, k_x and k_y, but up to a critical fraction of about a fifth of the unit cell. Scenarios marked in blue are the ones where bonds start cleaving on account of the narrowing lower-bias region. With larger supercells, the TI phase emerges at a lower voltage for the same biased fraction. Thus, with realistically larger supercells, implying a larger separation and width of the parallel gates, the TI phase may be accessible at lower bias potentials, well within the limit of sustainability of the monolayers.

3.4. Topological transition in electrically strained Xane ribbons

In the case of ribbons, we have two options for placing the gates – perpendicular or parallel to the ribbons. Gates perpendicular to the ribbons would induce tensile strain along the length of the ribbons, which will be substantially compensated by shrinkage of width due to free edges, leading to lesser bond

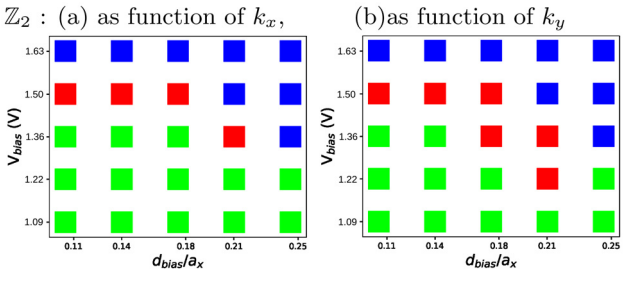

Fig. 8 Map of emergence of $\mathbb{Z}_2$ oddness (marked in red) for different bias amplitudes (V_{bias}) and fractions of the unit cell over which the bias is applied, for the germanane supercell (Fig. 1(a)). Marked in green are scenarios where the system remains trivial. Marked in blue are scenarios where bonds in the system start cleaving.

This journal is © The Royal Society of Chemistry 2025

Open Access Article. Published on 29 August 2025. Downloaded on 5/5/2026 7:59:23 AM.
This article is licensed under a Creative Commons Attribution-NonCommercial 3.0 Unported Licence.

strains. Additionally, ribbon edges at regions of higher bias would substantially buckle, causing structural degeneration. We thus realistically only consider gates parallel to the ribbons. With the electric field preferred in the ZZ direction for optimal distribution of strain, the choice for ribbons with gates parallel to them must be armchair edged. If we consider a linear gate embedded beneath the ribbons along their length and mid-way across their width, then we need to apply negative bias (Fig. 9(a)) so that the X–X bonds transverse to the ribbon direction can undergo the tensile strain needed for the TI phase. We have considered a Gaussian switching of potential to zero from the peak in the middle across the width of the ribbon. Low shrinkage of the unit cell along the length of the ribbon indicates substantial retention of the tensile strain of the X–X bonds transverse to the ribbons. However, strain cannot be induced uniformly across the width due to the tension released by the free edges, as is evident from the bond-length profile in Fig. 9(b). Tension can of course be imagined to be maintained by pulling the ribbon outward transverse to the ribbon through additional parallel positively biased gates on two sides. However, in this work, we limit our consideration to the effect of only one negatively biased linear gate parallel to the ribbon embedded halfway across the width (Fig. 9(a)). As is evident in Fig. 9(c), increasing the negative bias causes substantial lowering of the band-gap driven by the electrically induced tensile strain, similar to what happens in the monolayer. The bond-length distribution (Fig. 9(b)) shows that with increasing bias strength, the maximum tensile strain occurs halfway across the width, paving the way for the possibility of a TI phase to emerge over a fraction of the width of the ribbon symmetrically about the gate. The unit cell would thus be partitioned into TI and OI regions, implying the appearance of chiral interface states localizing intermediately between the halfway point and edge on two sides. Within the range of width of ribbons that we could compute using the resources at our disposal, we present promise that for sufficiently larger widths and appropriate selection of bias, it will be possible to induce topologically protected chiral interface states at Γ. For the ribbon depicted in Fig. 9, we indeed see localization of the VBE, but only an onset of asymmetry of the CBE within the bias sustained by the ribbon. This is expected, since the highest bond-length occurring in the middle of the ribbon did not exceed 2.7 Å, which appears to be a threshold bond-length for SOC to consolidate sufficiently, as per the emergence of the TI phase in the germanane monolayer. Promise is borne by the increasing difference in peak heights (Fig. 10) of the VBE and CBE localizing at the two interfaces. For germanane ribbons, an appreciable difference is observed in ribbons with a width of above 100 Å (Fig. 10(a)). Expectedly, for stanane ribbons a similar population difference is observed at a smaller width of less than 100 Å (Fig. 10(b)). The observed spatial separation of the degenerate VBE and VBE−1 and similarly of the CBE and CBE + 1 around Γ (marked as Γ + Δk in Fig. 10) indicates the onset of consolidation of the TI phase within the region of lower bias. These

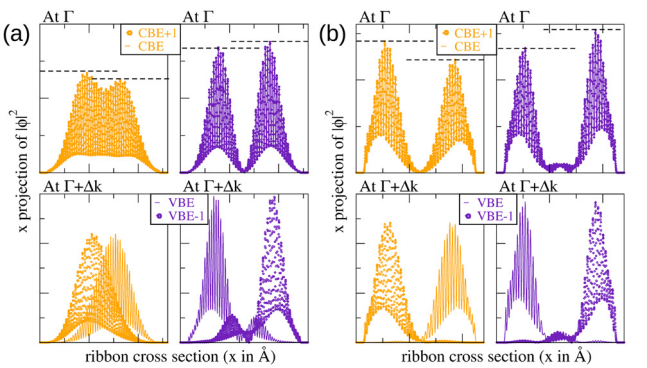

Fig. 10 Projection of the CBE + 1, CBE, VBE and VBE−1 at Γ and Γ + Δk, plotted for (a) a germanane ribbon with a width of more than 100 Å (24 zigzag units) with V_{bias} = −1.50 V applied halfway along the AC edge (Fig. 9(a)), and (b) a stanane ribbon with a width of less than 100 Å (20 zigzag units) with V_{bias} = −0.34 V applied.

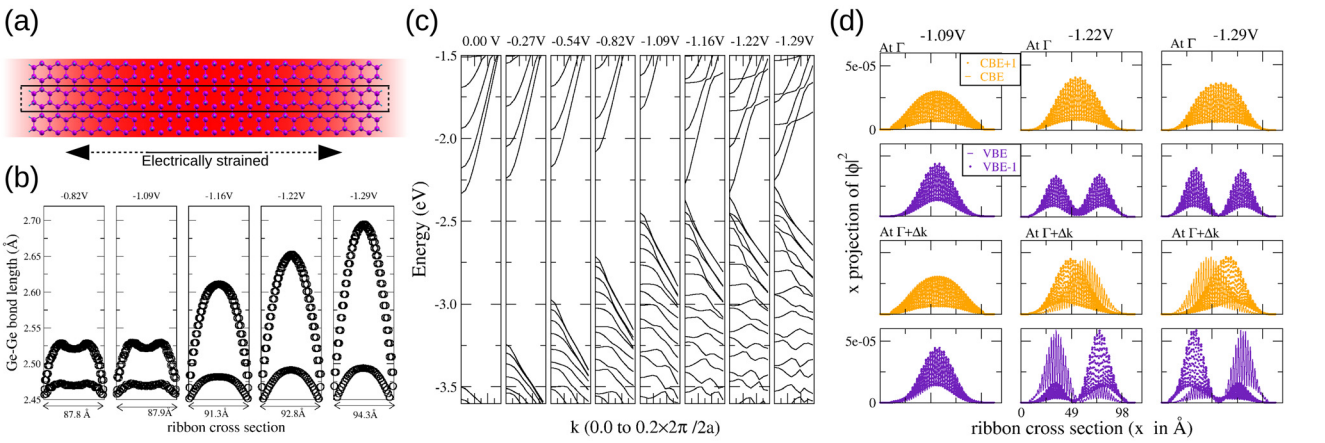

Fig. 9 (a) Inhomogeneously biased germanane ribbon with a width of 20 zigzag units. The inhomogeneity of the applied negative bias is depicted as a 2D contour in the background. (b) Ge–Ge average bond length plotted along the ribbon cross-section. (c) Band structures of the inhomogeneously biased germanane ribbon with increasing V_{bias}. (d) CBE + 1, CBE, VBE and VBE−1 at Γ and Γ + Δk, plotted for increasing V_{bias}.

Open Access Article. Published on 29 August 2025. Downloaded on 5/5/2026 7:59:23 AM.
This article is licensed under a Creative Commons Attribution-NonCommercial 3.0 Unported Licence.

results suggest the possibility to reversibly induce a linear channel of TI region with chiral interface states within realizably large monolayer segments exclusively through application of negative bias minimally at a single linear gate embedded underneath.

To substantiate this possibility, we again resort to the gapped-graphene ribbon heterostructure model system (Fig. 11), made of two regions akin to that considered for the monolayer. To associate the TI nature with the region in the middle (R1) within the Kane–Mele model (eqn (1)), we increase the magnitude of $|t_{nnn}|$ around its analytic threshold for onset of the TI phase, which is $|t_0| = m/(3\sqrt{3}) = 0.1347$ eV, where m is the mass term, set to 0.7 eV.[30] The electronic structure in the model is completely sectorized in the two spins since we have not included any Rashba term in our model. As is evident in Fig. 11, with increasing $|t_{nnn}|$ beyond $|t_0|$, the VBE and CBE at Γ start localizing at the interface of the two regions. However, chiral separation of the VBE and CBE to the two interfaces at Γ starts at a much higher $|t_{nnn}|$, which is expected to reduce with increasing width of R1. In agreement with the observed spatial separation of the degenerate VBEs and CBEs at Γ + Δk in partially biased germanane and stanane ribbons (lower panels of Fig. 9(d) and 10), in this model also, the VBEs and CBEs of the two spin sectors at Γ + Δk (panel at the bottom of Fig. 11) and their Kramer pairs at Γ − Δk start localizing separately at the two interfaces immediately once $|t_{nnn}|$ exceeds $|t_0|$.

At a much higher value of $|t_{nnn}|$, in excess of about 0.25 eV, we start observing chiral separation of the VBE and CBE, implying equivalence of the paradigm of partially biased Xane ribbons promised above with a TI channel embedded within. In fact, the location of the interface within the half-width of the ribbon can be custom defined by adjusting the amplitude of the applied bias.

It is pertinent to note here the adverse impact on the onset of the TI transition due to many-electron effects amounting to quasi-particle (QP) correction,[35,36] which is known to increase the band-gap through improvement in the description of screening and is not factored in due to its prohibitive computational cost for the size of unit cells considered in this work. Therefore, our results in principle present a plausibility study of the emergence of the TI phase in inhomogeneously biased Xane monolayers and ribbons. However, the typical range of QP correction in Xenes being in the range of 1 eV–1.5 eV,[18,37] the comparable reduction in band-gap as a function of bias difference found in this work holds promise that the emergence of the TI phase demonstrated here will be possible in realistically larger gate and supercell configurations in the presence of many-electron effects.

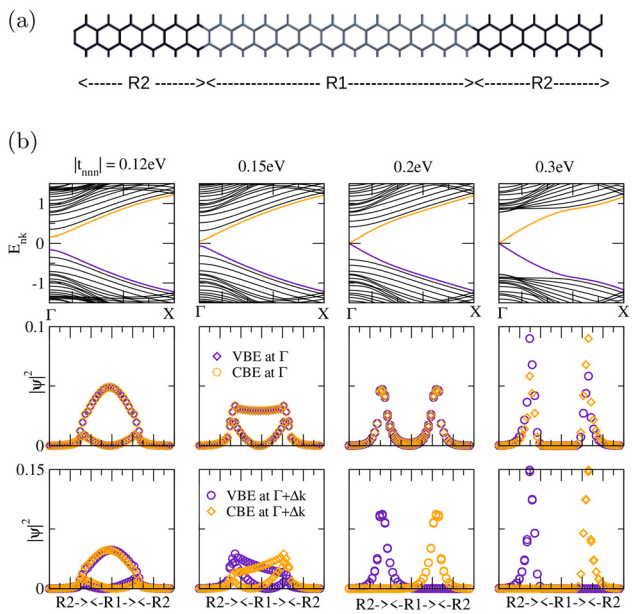

Fig. 11 (a) Unit cell of the gapped-graphene ribbon model system with two regions R1 and R2. (b) Band-structure and charge density of the valence and conduction band edges at Γ and a neighboring point Γ + Δk.

4. Conclusion

We have computationally demonstrated from first principles an exclusively electrical means to reversibly induce strain and tune band-structure, down to gap closure and band inversion at the TRIM, followed by emergence of a topologically insulating (TI) phase in monolayers and ribbons of heavier hydrogenated Xenes (Xanes), namely germanane and stanane, through application of inhomogeneous bias using gates of realizable length scale. The key underlying mechanism is band inversion through interplay of the non-relativistic energetics of interatomic tunelling and Coulomb repulsion owing to the variable strain in X–X bonds in regions of different bias, followed by opening of the band-gap caused by consolidation of spin–orbit coupling due to tensile strain in the region of lower bias. Band inversion is also accompanied by a spatial swapping of localization of the conduction and valence bands at the TRIM among regions of different bias. In sufficiently wide ribbons of these Xanes with negatively biased linear gates embedded midway and parallel to them, a TI region may emerge over a fraction of the width, with topologically protected chiral interface states customizably localizable with the half-width. Kramers' degenerate pairs of states from the valence and conduction bands about Γ start localizing at the two interfaces separately for workably lower voltages and narrower ribbons, and thus should be easily accessible. The demonstrated possibility of an electrically induced topological insulator phase should be realizable in the broad class of two-dimensional materials with p-orbitals as frontier orbitals.

Conflicts of interest

There are no conflicts to declare.

This journal is © The Royal Society of Chemistry 2025

Open Access Article. Published on 29 August 2025. Downloaded on 5/5/2026 7:59:23 AM. This article is licensed under a Creative Commons Attribution-NonCommercial 3.0 Unported Licence.

Data availability

All relevant data are presented in the manuscript.

Acknowledgements

Computations have been performed using facilities funded by the Dept. of Atomic Energy (DAE) of the Govt. of India (GOI). JB acknowledges generous funding support from grant no. RIN4001 from the DAE, GOI.

References

1 K. S. Novoselov, A. K. Geim, S. V. Morozov, D. Jiang, Y. Zhang, S. V. Dubonos, I. V. Grigorieva and A. A. Firsov, Electric field effect in atomically thin carbon films, *Science*, 2004, **306**(5696), 666–669.
2 S. D. Sarma, S. Adam, E. H. Hwang and E. Rossi, Electronic transport in two-dimensional graphene, *Rev. Mod. Phys.*, 2011, **83**(2), 407–470.
3 S. Balendhran, S. Walia, H. Nili, S. Sriram and M. Bhaskaran, Elemental analogues of graphene: silicene, germanene, stanene, and phosphorene, *Small*, 2015, **11**(6), 640–652.
4 L. Tao, E. Cinquanta, D. Chiappe, C. Grazianetti, M. Fanciulli, M. Dubey, A. Molle and D. Akinwande, Silicene field-effect transistors operating at room temperature, *Nat. Nanotechnol.*, 2015, **10**(3), 227–231.
5 A. Acun, L. Zhang, P. Bampoulis, M. v. Farmanbar, A. van Houselt, A. N. Rudenko, M. Lingenfelder, G. Brocks, B. Poelsema, M. I. Katsnelson, *et al.*, Germanene: the germanium analogue of graphene, *J. Phys.: Condens. Matter*, 2015, **27**(44), 443002.
6 J.-K. Lyu, S.-F. Zhang, C.-W. Zhang and P.-J. Wang, Stanene: a promising material for new electronic and spintronic applications, *Ann. Phys.*, 2019, **531**(10), 1900017.
7 X. Duan, C. Wang, A. Pan, R. Yu and X. Duan, Two-dimensional transition metal dichalcogenides as atomically thin semiconductors: opportunities and challenges, *Chem. Soc. Rev.*, 2015, **44**, 8859–8876.
8 F. Zheng, W. Meng and L.-J. Li, Continue the scaling of electronic devices with transition metal dichalcogenide semiconductors, *Nano Lett.*, 2025, **25**(10), 3683–3691. PMID: 39992904.
9 M. Z. Hasan and C. L. Kane, Colloquium: Topological insulators, *Rev. Mod. Phys.*, 2010, **82**, 3045–3067.
10 M. S. Lodge, S. A. Yang, S. Mukherjee and B. Weber, Atomically thin quantum spin hall insulators, *Adv. Mater.*, 2021, **33**(22), 2008029.
11 K.-H. Jin, W. Jiang, G. Sethi and F. Liu, Topological quantum devices: a review, *Nanoscale*, 2023, **15**(31), 12787–12817.
12 L. Kou, B. Yan, F. Hu, S.-C. Wu, T. O. Wehling, C. Felser, C. Chen and T. Frauenheim, Graphene-based topological insulator with an intrinsic bulk band gap above room temperature, *Nano Lett.*, 2013, **13**(12), 6251–6255.
13 J. Han, A. Richardella, S. A. Siddiqui, J. Finley, N. Samarth and L. Liu, Room-temperature spin-orbit torque switching induced by a topological insulator, *Phys. Rev. Lett.*, 2017, **119**(7), 077702.
14 S. Chen, I. J. Parker and B. Monserrat, Temperature effects in topological insulators of transition metal dichalcogenide monolayers, *Phys. Rev. B*, 2024, **109**(15), 155125.
15 P. Bampoulis, *et al.*, Quantum spin hall states and topological phase transition in germanene, *Phys. Rev. Lett.*, 2023, **130**, 196401.
16 D. J. Klaassen, I. Boutis, C. Castenmiller and P. Bampoulis, Tunability of topological edge states in germanene at room temperature, *J. Mater. Chem. C*, 2024, **12**(39), 15975–15980.
17 E. Bianco, S. Butler, S. Jiang, O. D. Restrepo, W. Windl and J. E. Goldberger, Stability and exfoliation of germanane: a germanium graphane analogue, *ACS Nano*, 2013, **7**(5), 4414–4421.
18 P. Lu, L. Wu, C. Yang, D. Liang, R. Quhe, P. Guan and S. Wang, Quasiparticle and optical properties of strained stanene and stanane, *Sci. Rep.*, 2017, **7**(1), 3912.
19 C. Si, J. Liu, Y. Xu, J. Wu, B.-L. Gu and W. Duan, Functionalized germanene as a prototype of large-gap two-dimensional topological insulators, *Phys. Rev. B: Condens. Matter Mater. Phys.*, 2014, **89**, 115429.
20 J. E. Padilha, L. B. Abdalla, A. J. R. da Silva and A. Fazzio, Fully and partially iodinated germanane as a platform for the observation of the quantum spin hall effect, *Phys. Rev. B*, 2016, **93**, 045135.
21 Y. Ma, *et al.*, Strain-induced quantum spin hall effect in methyl-substituted germanane $gech_3$, *Sci. Rep.*, 2014, **4**, 7297.
22 T. Teshome and A. Datta, Strain-induced topological insulator in methyl-decorated sige films, *J. Phys. Chem. C*, 2018, **122**(43), 25127–25133.
23 J. Qi, X. Li and X. Qian, Electrically controlled band gap and topological phase transition in two-dimensional multilayer germanane, *Appl. Phys. Lett.*, 2016, **108**(25), 253107.
24 Y. Zhao and Z. Li, Tuning the bandgap and topological phase transition in bilayer van der Waals stanane by electric field, *Phys. Status Solidi RRL*, 2024, **18**(5), 2300496.
25 P. Giannozzi, *et al.*, Quantum espresso: a modular and open-source software project for quantum simulations of materials, *J. Phys.: Condens. Matter*, 2009, **21**(39), 395502.
26 L. Fu and C. L. Kane, Time reversal polarization and a z 2 adiabatic spin pump, *Phys. Rev. B: Condens. Matter Mater. Phys.*, 2006, **74**(19), 195312.
27 A. A. Soluyanov and D. Vanderbilt, Wannier representation of Z_2 topological insulators, *Phys. Rev. B: Condens. Matter Mater. Phys.*, 2011, **83**, 035108.
28 A. A. Soluyanov and D. Vanderbilt, Computing topological invariants without inversion symmetry, *Phys. Rev. B: Condens. Matter Mater. Phys.*, 2011, **83**, 235401.
29 C. L. Kane and E. J. Mele, Quantum spin hall effect in graphene, *Phys. Rev. Lett.*, 2005, **95**, 226801.

Open Access Article. Published on 29 August 2025. Downloaded on 5/5/2026 7:59:23 AM.
This article is licensed under a Creative Commons Attribution-NonCommercial 3.0 Unported Licence.

30 D. Vanderbilt, *Berry Phases in Electronic Structure Theory: Electric Polarization, Orbital Magnetization and Topological Insulators*, Cambridge University Press, 2018.
31 I. Mayer, Charge, bond order and valence in the ab initio scf theory, *Chem. Phys. Lett.*, 1983, **97**(3), 270–274.
32 Y. Li and Z. Chen, Tuning electronic properties of germanane layers by external electric field and biaxial tensile strain: a computational study, *J. Phys. Chem. C*, 2014, **118**(2), 1148–1154.
33 X. Liu, Y. Wang, F. Li and Y. Li, Two-dimensional stanane: strain-tunable electronic structure, high carrier mobility, and pronounced light absorption, *Phys. Chem. Chem. Phys.*, 2016, **18**(21), 14638–14643.
34 M. Hossain, J. De and J. Bhattacharjee, Hybrid atomic orbital basis from first principles: Bottom-up mapping of self-energy correction to large covalent systems, *J. Phys. Chem. A*, 2021, **125**(31), 6805–6817. PMID: 34324816.
35 L. Matthes, S. Küfner, J. Furthmüller and F. Bechstedt, Intrinsic spin hall conductivity in one-, two-, and three-dimensional trivial and topological systems, *Phys. Rev. B*, 2016, **94**(8), 085410.
36 F. Matusalem, F. Bechstedt, I. Guilhon, M. Marques and L. K. Teles, Dft-1/2 method applied to 2d topological insulators: fluorinated and hydrogenated group-iv honeycomb systems, *J. Phys.: Condens. Matter*, 2021, **33**(43), 435501.
37 H. Shu, Y. Li, S. Wang and J. Wang, Quasi-particle energies and optical excitations of hydrogenated and fluorinated germanene, *Phys. Chem. Chem. Phys.*, 2015, **17**(6), 4542–4550.

 This journal is © The Royal Society of Chemistry 2025